Croatian Society for Materials Protection

Metalurgija/Metallurgy

Vol. 66 No. 1 / 2027

Investigation of the Solidification Rate in Twin-Roll Cast and Rolled Zr Microalloyed Al-Mg-Si Aluminum Alloys: a Molecular Dynamics Approach

Wenlin Gao[1,2,3,4], Junzhou Chen[1,3,4*], Ruijue Wang[2], Jicheng Wang[2], Feng Sun[2], and Chengning Li[5]

https://doi.org/10.64486/m.66.1.2

[1] AECC Beijing Institute of Aeronautical Materials, Beijing 100095, China
[2] Hexing Aeronautical Materials (Tianjin) Technology Co., Ltd., Tianjin 300399, China
[3] Beijing Engineering Research Center of Advanced Aluminum Alloys and Applications, Beijing 100095, China
[4] Advanced Aluminum Alloy Technology Innovation Center, Beijing 100095, China
[5] School of Materials Science and Engineering, Tianjin University, Tianjin, 300350, China
* Correspondence: cjz1231216@163.com

Type of the Paper: Article
Received: February 12, 2026
Accepted: May 9, 2026

Abstract: The present study investigated the impact of Zr microalloying on the solidification mechanism and rate of cast-rolled Al-Mg-Si aluminum alloy, using differential scanning calorimetry, light microscopy, and Pandat™ thermodynamic calculations. The molecular dynamics models of three different systems were established: Al-pure, Al-0.1Zr and Al-0.3Zr. The results revealed that an optimal amount of Zr effectively reduced the nucleation barrier at the atomic level during alloy solidification. This reduction facilitated the formation of critical nuclei, promoted the transformation of hexagonal close-packed clusters into face-centered cubic clusters, altered the mechanism of grain nucleation and growth, and enhanced the solidus temperature of the cast-rolled alloy. Consequently, the temperature range of the solid-liquid two-phase region was narrowed, leading to a substantial increase in the alloy's solidification rate. These atomic-scale findings enhance understanding of Zr's role in solidification control, offering a basis for designing high-performance aluminum alloys and guiding industrial twin-roll casting processes.

Keywords: molecular dynamics; twin-roll casting and rolling; solidification rate; aluminum alloy

1. Introduction

Al-Mg-Si aluminum alloy is an extensively used lightweight and high-strength aluminum alloy, which is known for its outstanding mechanical properties and corrosion resistance. It is widely applied in aerospace, transportation, and various industries [1-3], particularly in the production of aluminum alloy plates. Among the various methods for forming these plates, the twin-roll casting and rolling (TRCR) process has emerged as a streamlined and efficient approach, which minimizes intermediate manufacturing processes, resulting in energy and raw material savings [4,5]. However, the TRCR process faces challenges due to the large disparity in solidification rates between the plate edges and center, which can lead to defects such as segregation and cracks [6,7]. Microalloying is a strategic solution to address these issues, effectively enhancing sheet quality and structural plasticity [8].

Zhang et al. [9] reported that the addition of 0.06 wt.% Zr to gravity-cast aluminum alloys substantially reduces the secondary dendrite arm spacing, refines structural grains, and suppresses macrosegregation. Similarly, Pan et al. [10] demonstrated that the incorporation of 0.28 wt.% Zr element into 3003 aluminum alloy induces refinement of nanoprecipitated α-AlFeMnSi and Al3Zr phases under peak aging conditions, ultimately enhancing thermal stability. Zhang et al. [11] further established that the introduction of trace amounts of Zr to Al-Mg-Si cast-rolled aluminum alloys plays a crucial role in promoting the precipitation of β" strengthening phase, thereby improving the mechanical properties of the alloy. Collectively, the above findings as well as numerous other investigations confirm that Zr microalloying is an effective strategy for promoting grain refinement and precipitation hardening in aluminum alloys, thus enhancing their structural properties [12-14].

TRCR is a semi-solid forming technique that integrates both casting and rolling processes. In this method, the solidification rate plays a pivotal role in determining the solid phase fraction, directly affecting the quality of cast and rolled plates [15,16]. Current research efforts predominantly focus on assessing the influence of Zr microalloying on the properties of aluminum alloys. However, there is a notable absence of studies examining the impact of Zr microalloying on the solidification rate during aluminum alloy casting and rolling. Molecular dynamics stands out as a crucial methodology for studying microstructural evolution and solidification behavior at the atomic scale and for revealing the influence of microalloying elements on the solidification rate [17-20]. Building upon this foundation, the present work investigated the effect of Zr microalloying on the solidification rate of cast-rolled Al-Mg-Si alloy. By establishing the molecular dynamics model for the corresponding system, the influence mechanism of Zr microalloying on the solidification rate during the cast-rolling process is elucidated at the atomic level.

2. Materials and Methods

Raw materials for the present study included Al-10Mn and Al-10Zr master alloys, as well as 6061 aluminum alloy. The raw materials were placed in a furnace and the temperature was raised to 750 °C and maintained for 45 min. Subsequently, the casting and rolling process was performed using a Ø16 cm twin-roll horizontal casting mill, at a casting speed of 30 m/min, a pouring temperature of 680 °C, and a roll gap of 1.5 mm. Four Al-Mg-Si cast-rolled aluminum alloy plates with different Zr contents were prepared, and their compositions are detailed in Table 1. For metallographic analysis, samples were initially cold mounted in epoxy resin, then polished down to 1 μm, and subsequently electrochemically etched in a solution comprising 50 mL of H_2O and 200 mL of HBF_4. The metallographic structure of the cast-rolled plate samples was observed under polarized light using a ZEISS Axio Vert.A1 light microscope (LM), with the detection surface oriented along both rolling and thickness directions. To further characterize the alloy, a differential thermal analyzer (Setram Sesys Evolution) was employed. Prior to analysis, plate samples were processed by grinding into 30±5 mg aluminum alloy powder. During differential scanning calorimetry (DSC), the detection temperature range was between 25 ℃ and 800 ℃, argon was used as the protective gas, and the heating rate was set at 10 ℃/min.

Table 1. Chemical compositions of cast-rolled aluminum alloy plates/wt.%

Alloy	Mg	Si	Fe	Cu	Cr	Ti	Zn	Mn	Zr
1#	1.01	0.73	0.21	0.31	0.13	0.02	0.05	0.38	0
2#	1.03	0.75	0.22	0.32	0.15	0.03	0.04	0.40	0.09
3#	1.02	0.74	0.22	0.32	0.14	0.02	0.05	0.39	0.21
4#	1.04	0.73	0.23	0.30	0.14	0.03	0.04	0.42	0.32

The alloy composition was designed and non-equilibrium solidification calculations were conducted using Pandat™ thermodynamic calculation software. Molecular dynamics simulations of the isothermal crystallization process of Al and Al-Zr alloys were performed using the Lammps program package. Three distinct groups of component systems were established: the original pure aluminum system (labeled as Al-pure), the trace Zr element system (Al-0.1Zr), and the optimal Zr element system (Al-0.3Zr). The simulations were performed un-

https://doi.org/10.64486/m.66.1.2

der periodic boundary conditions within a cubic box containing 37,640 uniquely numbered atoms. The isothermal-isobaric ensemble (NPT) was employed to simulate the cooling and crystallization process of the alloy, with pressure control at (P = 0) according to the modified Nose-Hoover method [21]. The interatomic interactions were described using the Al-Zr Modified Embedded Atom Method (MEAM) potential developed by Rahele et al. [22], with the Al atom interaction potential created by B. Lee et al. [23]. Studies have confirmed that the melting point of pure Al calculated by the Al atom interaction potential developed by B. Lee et al. is approximately 925 K, which is considered a more accurate interaction potential energy [24]. The velocity-Verlet algorithm [25] was employed to solve the motion equations, with a time step set to 1 fs. The simulation process involved initial isothermal relaxation of the system at 1500 K to achieve equilibrium. Subsequently, the system was cooled to the selected temperature point at a cooling rate of 1.4×10^9 K/s. Finally, the system was isothermally relaxed for 500 ps at each chosen temperature point. During this period, data were collected every 1 ps to record the energy of the system and the spatial coordinates of each atom. The chosen temperature point was 500 K, whereas the corresponding sub-cooling degree ΔT_m was 0.46 × T_m.

The molecular dynamics simulations in this study were conducted on simplified Al-Zr binary systems rather than the full Al-Mg-Si-Mn-Zr composition used in the experiments. This simplification was deliberately chosen to isolate and elucidate the specific atomic-scale role of Zr in solidification kinetics. The presence of Mg and Si is known to significantly influence diffusion coefficients, solid-liquid interfacial energy, and clustering behavior in aluminum alloys. However, introducing multiple solute elements into the MD model would substantially increase the complexity of interatomic interactions, making it challenging to identify the individual contribution of Zr. Therefore, as a first-order approximation, this study focuses on the Zr-induced effects as a representative basis for understanding microalloying mechanisms. Future work will involve developing more comprehensive MEAM potentials to simulate the quinary system and validate the synergistic effects of Mg, Si, and Zr.

3. Results and Discussion

3.1. Thermodynamic calculations

Thermodynamic calculations were performed using Pandat™ software, which is renowned for its broad applicability, high accuracy, and robust scalability, and widely embraced by materials researchers and scholars [26,27]. Figure 1(a) presents the temperature change curve within the crystallization zone of the thermodynamically simulated Al-Mg-Si-0.4Mn alloy with varying Zr contents. As the Zr content increased, the liquidus line remained nearly constant around 650.1°C, while the solidus temperature increased from 582.7 °C to 599.6 °C. At a Zr content of 0.3 wt.%, the solidus temperature reached 590.8 °C, reducing the crystallization temperature range by 8.1 °C. Figure 1(b) shows the measured DSC temperature change curve of the Al-Mg-Si-0.4Mn plate, revealing a shortened crystallization interval by 4.73 °C - a trend consistent with the thermodynamic calculations. In general, the length of the solid-liquid two-phase zone influences the microstructure of the cast-rolled plate. An excessively wide crystallization zone may reduce the cooling rate around the roll gap, resulting in the accumulation of residual liquid in the center and causing central segregation [28]. Conversely, reducing the temperature within the solid-liquid two-phase region increases the cooling rate of the cast-rolled plate, accelerates the solidification rate, and ameliorates segregation, thereby enhancing structural uniformity.

The Pandat™ calculations presented here are based on the Scheil solidification model, which assumes no diffusion in the solid and complete mixing in the liquid. While this assumption may lead to quantitative deviations from the actual non-equilibrium solidification conditions during twin-roll casting, the primary purpose of these calculations is to establish the trend of solidus temperature variation with Zr content. As shown in Fig. 1, both the calculated and experimental DSC results consistently indicate that Zr addition narrows the solidification interval, providing a reliable macroscopic basis for subsequent atomic-scale investigation.

https://doi.org/10.64486/m.66.1.2

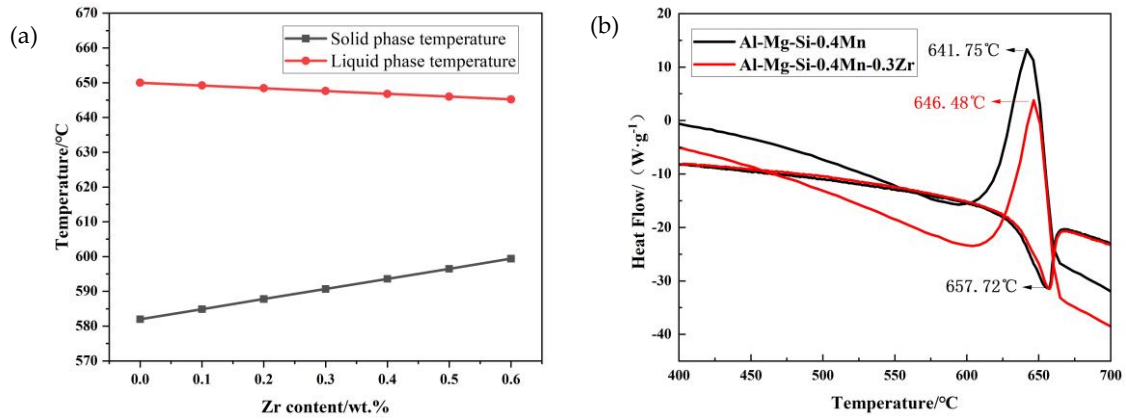

Figure 1. Thermodynamic calculation results of Al-Mg-Si alloy under Scheil conditions and the corresponding DSC temperature change curve within the solid-liquid temperature range of the alloy; (a) solid-liquid temperature change calculation curve, (b) DSC curve depicting temperature changes within the liquid temperature range

3.2. Microstructure

The combined presence of Mn and Zr synergistically suppressed recrystallization, thereby preserving the processing imprints within the aluminum alloy. As a result, the solidification degree of cast-rolled Al-Mg-Si alloy prior to rolling can be deduced from the metallographic structure after rolling [29]. In Figure 2, LM microstructural morphology of cast-rolled Al-Mg-Si-0.4Mn alloy plates with different Zr contents is presented along the rolling and thickness directions (RD-ND) [30]. This observation suggested that, with increasing Zr content, the rolling force applied on the plate increased. Relevant literature indicates that, during semi-solid processing, a higher solid phase fraction typically corresponds to greater rolling force [29]. The observed increase in rolling force is consistent with a higher solid fraction at the roll gap, which is promoted by Zr addition, as indicated by the thermodynamic calculations in Section 3.1.

With the addition of 0.3 wt.% Zr, both the solidification rate and solid phase fraction increased. Higher solid fractions were associated with elevated stress during processing. Consequently, the rolling force exerted on plates 2~4# surpassed that on plate 1#, with plate 4# exhibiting the greatest rolling force. The solidification diagrams of the original Al-Mg-Si cast-rolled plate and the Al-Mg-Si cast-rolled plate after Zr addition are shown in Figure 3(a) and (b), respectively [31]. The semi-solid deformation zone of the plate with an appropriate amount of Zr addition during the rolling process was notably longer, and the solid phase fraction of the plate was larger. The inhibitory influence of Mn and Zr on recrystallization induced a transformation in the microstructural morphology from Figure 3(c) to 3(d). As noted earlier, the combined presence of Mn and Zr synergistically impedes recrystallization, effectively preserving the deformation-induced fibrous microstructure. Therefore, while the final grain morphology is influenced by multiple factors (including temperature, deformation, and recrystallization), the enhanced grain elongation observed in Figure 2, together with the retained fibrous structure, indicates that Zr microalloying increases the solidification rate, leading to a higher solid fraction and greater rolling forces during the cast-rolling process.

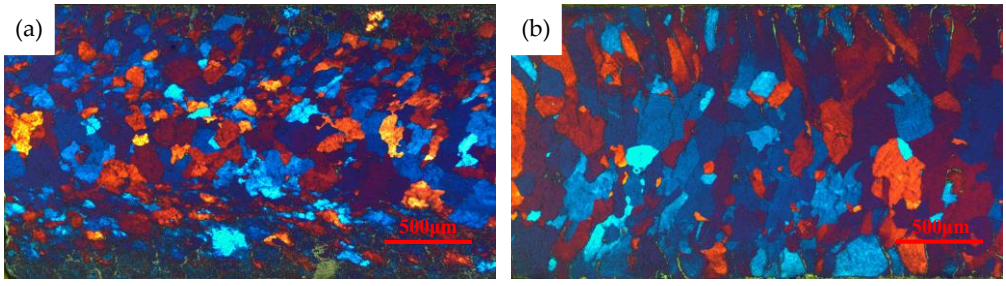

https://doi.org/10.64486/m.66.1.2

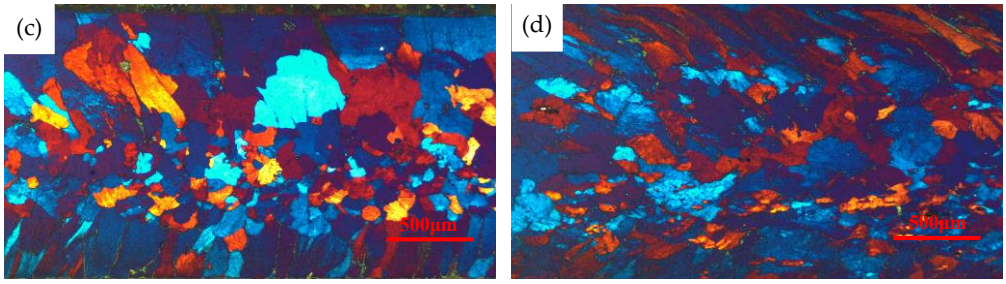

Figure 2. LM micrographs of microstructural morphology of cast-rolled Al-Mg-Si-0.4Mn alloys with different Zr contents [30]; (a) alloy 1#, (b) alloy 2#, (c) alloy 3#, (d) alloy 4#

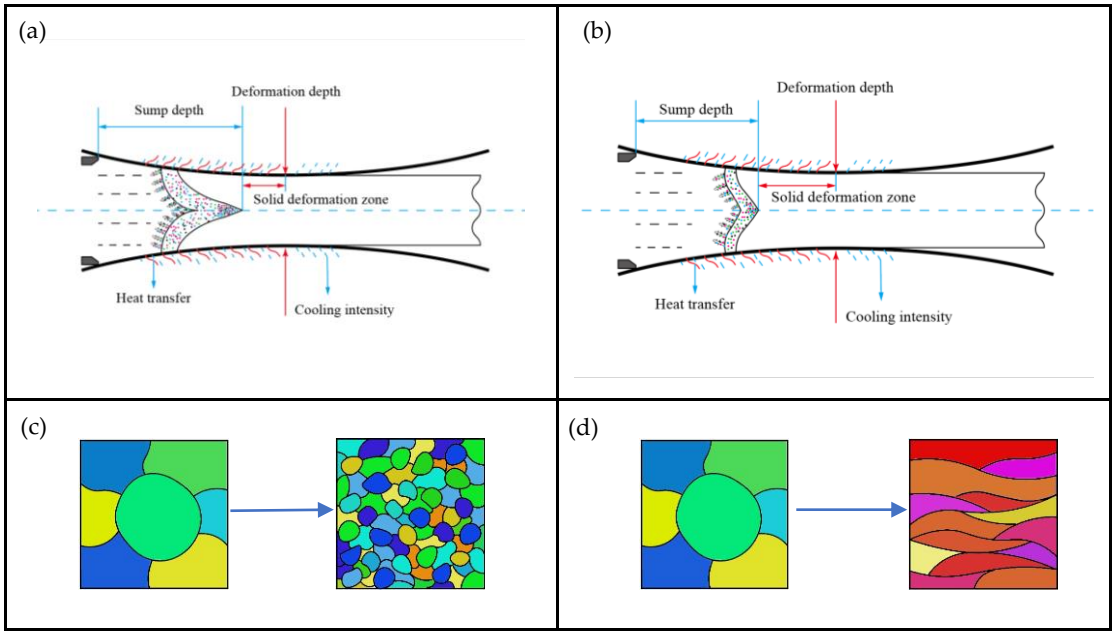

Figure 3. Al-Mg-Si cast-rolling solidification process diagram [31]; (a) original Al-Mg-Si cast-rolled plate solidification interval, (b) Al-Mg-Si cast-rolled plate solidification interval after Zr addition, (c) plate center change diagram, and (d) plate edge change diagram

3.3. Molecular dynamics analysis

The above thermodynamic calculation results and microstructural analysis demonstrated that Zr microalloying markedly increased the solidification rate of cast-rolled Al-Mg-Si alloy. To delve deeper into the underlying mechanism, a molecular dynamics model under cryogenic conditions was employed to simulate the solidification of aluminum alloys at the atomic level under varying Zr microalloying conditions. The solidification interval of average atomic energy of alloys with different Zr contents was plotted as a function of relaxation time (t). To discern the time intervals of thermodynamic phase transitions, the first-order derivative of energy ($\partial E/\partial t$) was calculated for each of the three systems. The energy mutation time points during crystallization under different systems are shown in Table 2 and Figure 4. Here, t_s and t_e denote the start and end times of crystallization, respectively, while t_m represents the time node when the energy decreases most rapidly. The results from Table 2 reveal that the addition of Zr led to varying degrees of reduction in crystallization time. When a trace amount of Zr was introduced, the crystallization time was approximately 30 ps, which is 26 ps shorter than the crystallization time of the Al-pure system. With an appropriate amount of Zr addition, the crystallization time decreased to around 27 ps, reflecting a 29 ps reduction in the crystallization time in comparison with the Al-pure system. Thus, the addition of different Zr contents shortened the solidification time required to achieve the fastest solidification rate by 4 and 12 ps, respectively. Consequently, it can be concluded

https://doi.org/10.64486/m.66.1.2

that the incorporation of an appropriate amount of Zr significantly accelerated the cryogenic solidification rate of aluminum alloys.

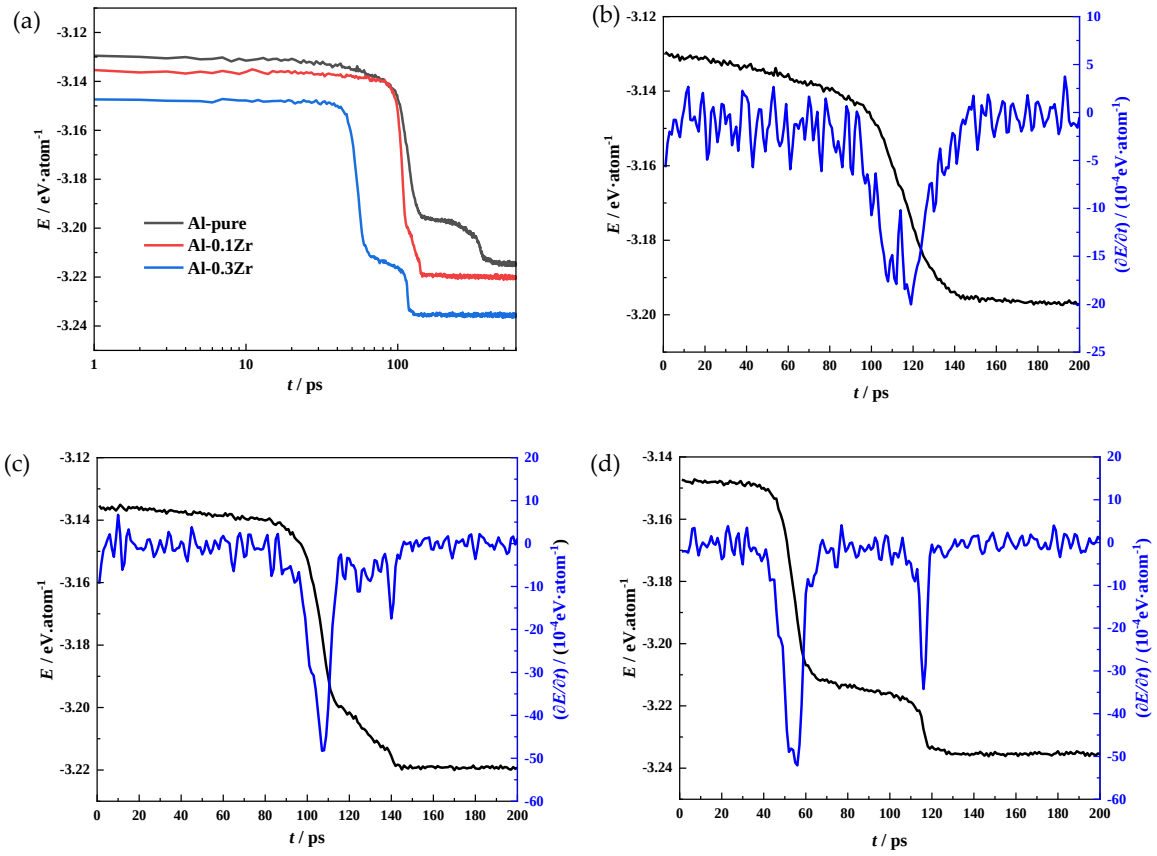

Figure 4. Variation in the average atomic energy of alloys with different Zr contents as a function of relaxation time (*t*); (a) total, (b) Al-pure, (c) Al-0.1Zr, and (d) Al-0.3Zr

Table 2. Energy mutation time points corresponding to the crystallization process in three different systems

t/ps	System		
	Al-pure	Al-0.1Zr	Al-0.3Zr
t_s	93	86	41
t_e	149	116	68
t_m	119	108	55

The microstructure evolution of the three systems during the crystallization process is illustrated in Figure 5, with curves depicting the number of atoms in the fcc, hcp, and bcc cluster structures as a function of relaxation time. The fcc cluster exhibited the highest number and dominance, followed by the hcp cluster, while the number of atoms in the bcc cluster was negligible. In the early stages of the solidification process, the quantity of atoms within the three clusters experienced rapid growth and stabilized over a certain period. With increasing relaxation time, the number of atoms in hcp clusters within the system gradually diminished while the number of atoms in fcc clusters continued to increase. This observation signified a transformation from hcp to fcc clusters. Moreover, the introduction of Zr intensified this phase transition phenomenon. When an appropriate amount of Zr was incorporated, the hcp structure in the system underwent nearly complete conversion into an fcc structure. Consequently, the addition of Zr facilitated transformation of hcp to fcc structure during solidification.

https://doi.org/10.64486/m.66.1.2

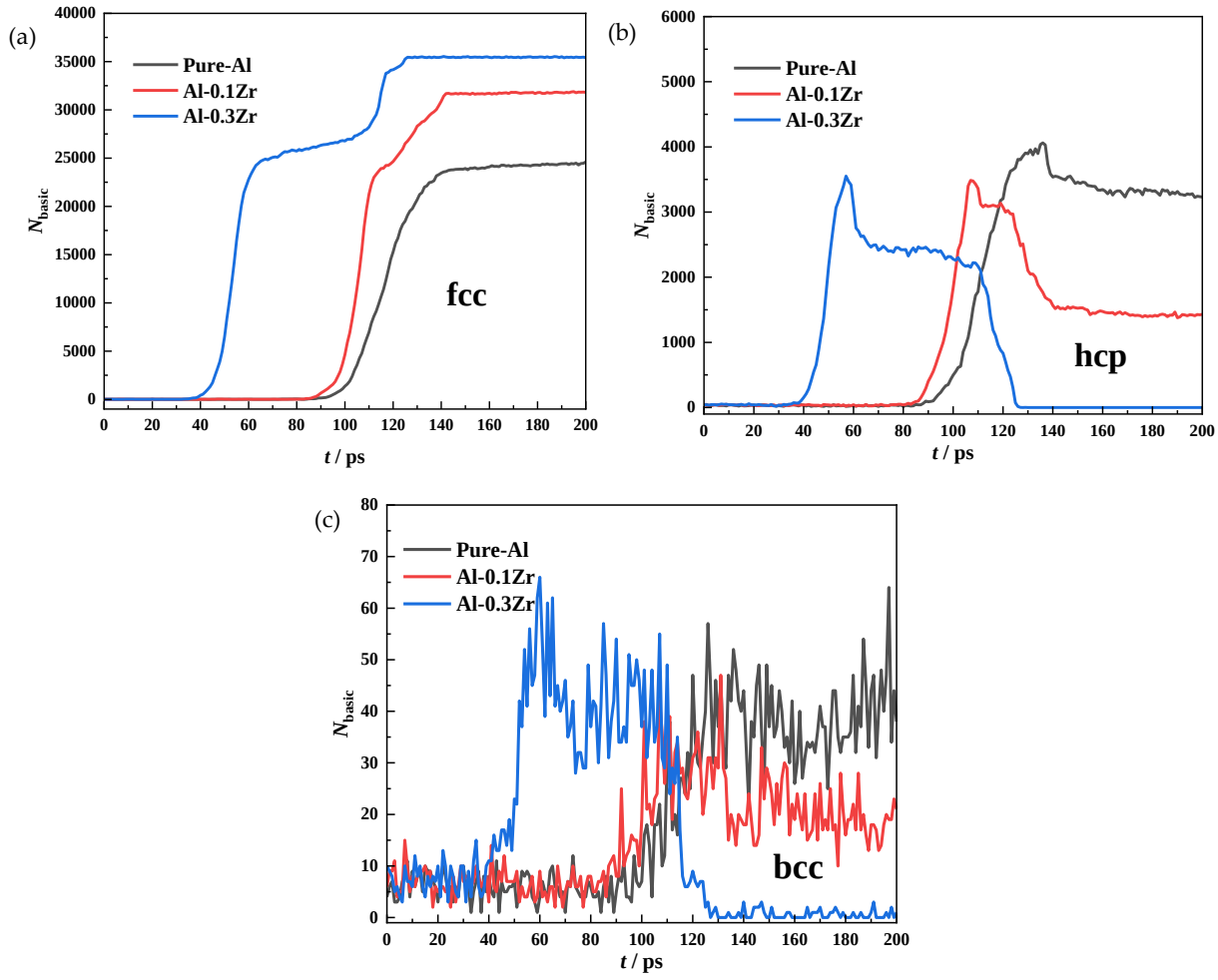

Figure 5. Variation of the basic cluster number N_{basic} of fcc, hcp, and bcc with relaxation time (t) for different Zr contents; (a) fcc, (b) hcp, and (c) bcc

The variations in the number of fcc single crystal clusters, denoted as q_{scc}, and the average cluster size with relaxation time are shown in Figure 6. With an increase in relaxation time, the number of single crystal clusters in the three systems first increased followed by the subsequent decline. In general, the crystallization process can be divided into nucleation and growth stages. The relaxation time node corresponding to the maximum number of clusters was labeled as t_{mx}. For relaxation times $t<t_{mx}$, there was an instantaneous increase in the number of clusters along with a concurrent growth in cluster size. This indicated that the nucleation process in the melt occurred prior to t_{mx}, leading to the formation of numerous crystal blanks and nuclei that gradually grew with relaxation time. For relaxation times $t>t_{mx}$, the number of single crystal clusters began to decrease, while the average cluster size underwent exponential growth. This signified a rapid growth of single-crystal clusters through aggregation. Simultaneously, Zr microalloying facilitated the transformation of hcp to fcc structure, enhancing the overall content of fcc structure. Consequently, clusters of the same type could aggregate, further accelerating the solidification rate.

https://doi.org/10.64486/m.66.1.2

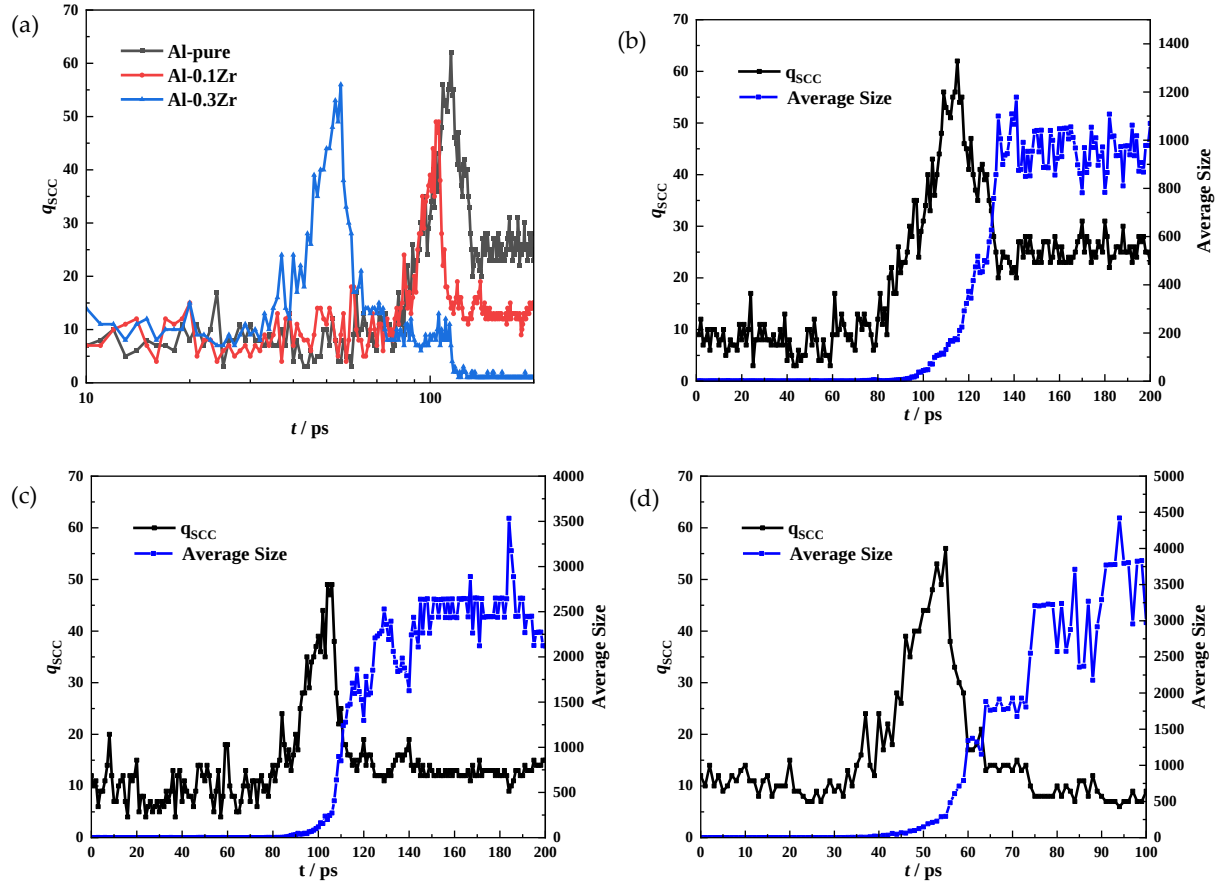

Figure 6. Number of single crystal clusters (q_{scc}) and change in the average cluster size with relaxation time (t); (a) total, (b) Al-pure, (c) Al-0.1Zr, and (d) Al-0.3Zr

To comprehensively investigate the influence of Zr on the nucleation of cryogenic liquid aluminum, the present study focused on analyzing the nucleation process throughout crystallization. The calculation equation for the nucleation barrier in the classical nucleation theory is as follows [32]:

$$\Delta G_c = \frac{4\alpha^3\gamma^3}{27(\rho\Delta\mu)^2} \tag{1}$$

In Eq. (1), ρ is the crystal atomic number density, $\Delta\mu$ is the chemical potential per atom, γ is the solid–liquid interfacial energy, and α is the nucleus shape factor. In general, the difficulty in precise measurement of γ and α poses a challenge in accurately calculating the nucleation barrier, ΔG_c, using Eq. (1). Therefore, in order to calculate the nucleation barrier, the present study employed Eq. (2) for steady-state nucleation rate and Eq. (3) for the steady-state nucleation rate definition.

$$I_0 = K \cdot exp\left(-\frac{\Delta G_c}{K_B T}\right) \tag{2}$$

$$I_0 = (\partial N_{nuclei}/\partial t)/V \tag{3}$$

In Eqs. (2) and (3), K is the kinetic prefactor, usually related to the self-diffusion coefficient and adsorption rate [33], N_{nuclei} is the total number of critical nuclei identified at time t. Since I_0 mainly depends on ΔG_c, the kinetic prefactor, K, was assumed to be a constant, unaffected by temperature, and V is the simulation volume. Using the following approximations: $\Delta\mu = \Delta H_m \Delta T_m / T_m$ and $\gamma = \gamma_m T / T_m$ [34,35], Eq. (2) can be rewritten as:

$$I_0 = K \cdot exp\left(-\frac{4\alpha^3\gamma m^3 T^2}{27 K_B T_m \rho^2 \Delta H_m^2 \Delta T_m^2}\right) \tag{4}$$

https://doi.org/10.64486/m.66.1.2

In the present analysis, the solid-liquid interfacial energy (γ) is not imposed as an a priori constant. Instead, the nucleation barrier ΔG_c—which implicitly incorporates γ along with other factors such as atomic mobility and chemical potential—is obtained by fitting the steady-state nucleation rates extracted directly from the MD simulations. As shown in Figure 7 and Table 3, the relationship between ln(I_0) and $T^2/\Delta T_m^2$ for the pure Al system was first established to determine the kinetic pre-factor K. Subsequently, the ΔG_c values for the Al-Zr systems were calculated using their respective simulated ln(I_0) values. This fitting-based approach ensures that any influence of Zr on interfacial energy, diffusivity, or local atomic ordering is self-consistently embedded in the final ΔG_c values, without requiring an explicit assumption about the numerical value of γ.

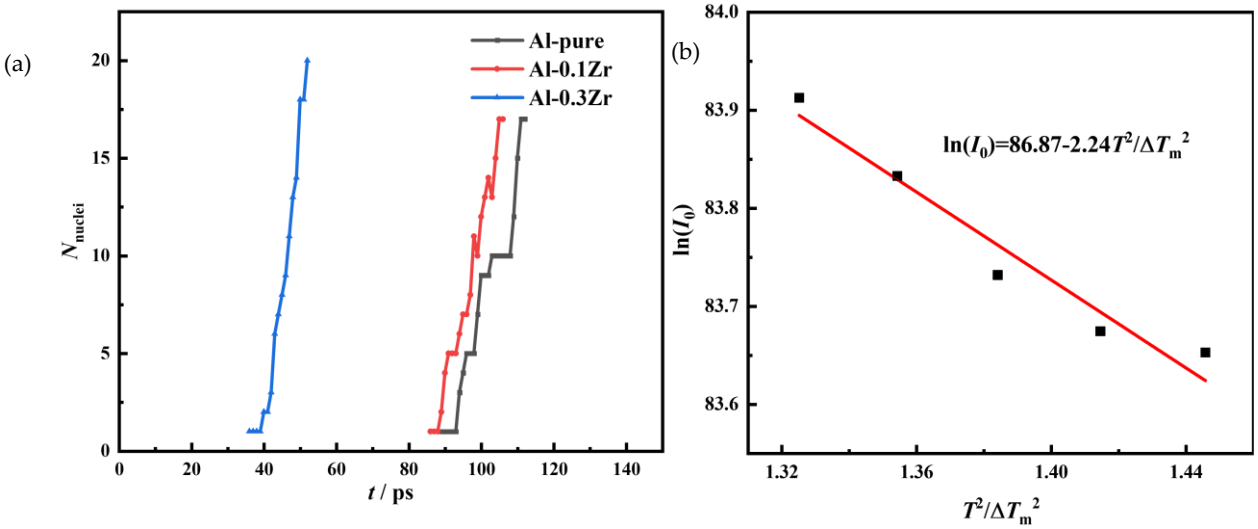

Figure 7. Determination of critical nucleus and nucleation barrier; (a) change in the critical nucleus number, N_{nuclei}, with relaxation time (t), (b) fitting curve of ln (I_0) and $T^2/\Delta T_m^2$

Table 3. ln (I_0) and $T^2/\Delta T_m^2$ in the temperature range of 495 K-505 K

Relaxation temperature/K	ln (I_0)	$T^2/\Delta T_m^2$
495	83.91	1.151
497.5	83.83	1.164
500	83.73	1.176
502.5	83.67	1.189
505	83.65	1.202

B. Shen et al. [36] reported that, when the nucleation system contains 55 fcc atoms, it can be considered a critical nucleus. On this basis, the present study utilized the nearest neighbor screening method to analyze the nucleation degree of the system. The variation in the critical nucleation number, N_{nuclei}, with relaxation time under different systems is shown in Figure 7(a). Only a slight difference was observed in the nucleation rate between Al-0.1Zr and Al-pure systems. However, with an increase in the Zr content, the nucleation rate increased, accompanied by a corresponding rise in nucleation time. Eq. (4) describes the relationship $\Delta G_c = (\ln K - \ln I_0)\, k_B T$. Through curve fitting of the MD calculation results (Table 3), the relationship between ln(I_0) and $T^2/\Delta T_m^2$ was derived during relaxation in the micro-zone temperature of 495 K-505 K in the Al-pure system. Consequently, K was calculated to be approximately 5.33×10^{37} $m^{-3}s^{-1}$ and $\ln K = 86.87$. Data from Table 4 showed that the nucleation barrier in the Al-pure system was around 3.137 $k_B T$. Upon addition of a trace amount of Zr, the nucleation barrier remained largely unchanged at about 3.149 $k_B T$. However, when an appropriate amount of Zr was introduced, the nucleation barrier decreased to approximately 2.979 $k_B T$. The schematic diagram of the nucleation barrier is illustrated in Figure 8. In summary, adding an optimum amount of Zr effectively reduced the nucleation barrier of aluminum alloy during cryogenic solidification, consequently increasing its solidification rate.

https://doi.org/10.64486/m.66.1.2

The nucleation barrier values presented in Table 4 are derived from a fitting procedure that assumes a constant kinetic pre-factor K, determined from the pure Al system. This approach is commonly adopted in the literature [33], but it introduces some uncertainty into the absolute values of ΔG_c, as K may theoretically vary with alloy composition. However, the primary conclusion of this study—that optimal addition of Zr (0.3 wt.%) reduces the nucleation barrier—is supported by the relative trend observed across the three systems. Even considering potential uncertainties in K, the consistently lower ΔG_c value for the Al-0.3Zr system compared to Al-pure and Al-0.1Zr strongly suggests that Zr promotes nucleation kinetics. Future work can incorporate more rigorous sensitivity analyses or direct measurements of K to further validate these findings.

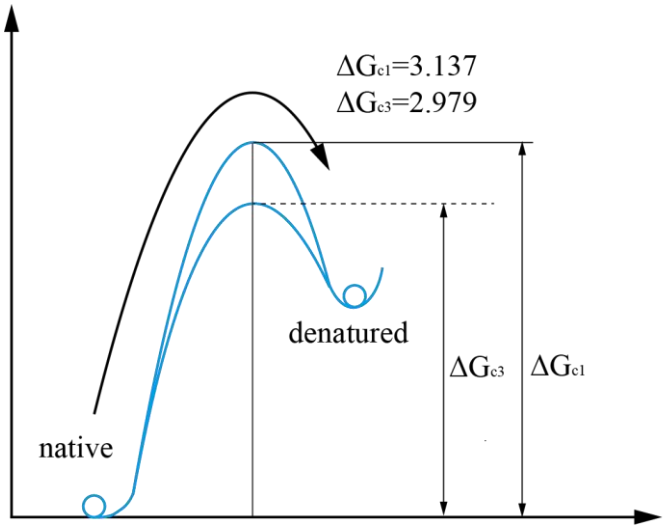

Figure 8. Nucleation barrier diagram

Table 4. ln(I_0) and nucleation barrier, ΔG_c, in different systems

System	Ln(I_0)	$\Delta G_c/k_BT$
Al-pure	83.732	3.137
Al-0.1Zr	83.720	3.149
Al-0.3Zr	83.890	2.979

The temporal evolution of the crystallization process in Al-pure and Al-0.3Zr systems is compared in Figure 9. For clarity, only fcc atoms are displayed, with the zero-moment defined as the 1 % solidification state. As seen from the figure, several spherical crystal nuclei appeared in the system at time 0. Subsequently, the surrounding fcc atoms swiftly adhered to these nuclei, promoting rapid growth. The majority of the single crystal clusters remained stable and continued expanding, showcasing a continuous and coordinated crystallization process. Upon introduction of Zr, there was a notable acceleration in the growth rate of clusters. During the middle stage of solidification, clusters experienced accelerated growth through aggregation, further enhancing the overall solidification rate. By the 20 ps mark, the solidification state in the Al-pure system reached 28.3 %, while in the Al-0.3Zr system, it reached 60.6 %. This observation highlights that the introduction of an optimal amount of Zr substantially reduces the solidification time of the system, leading to a significant increase in the solidification rate.

https://doi.org/10.64486/m.66.1.2

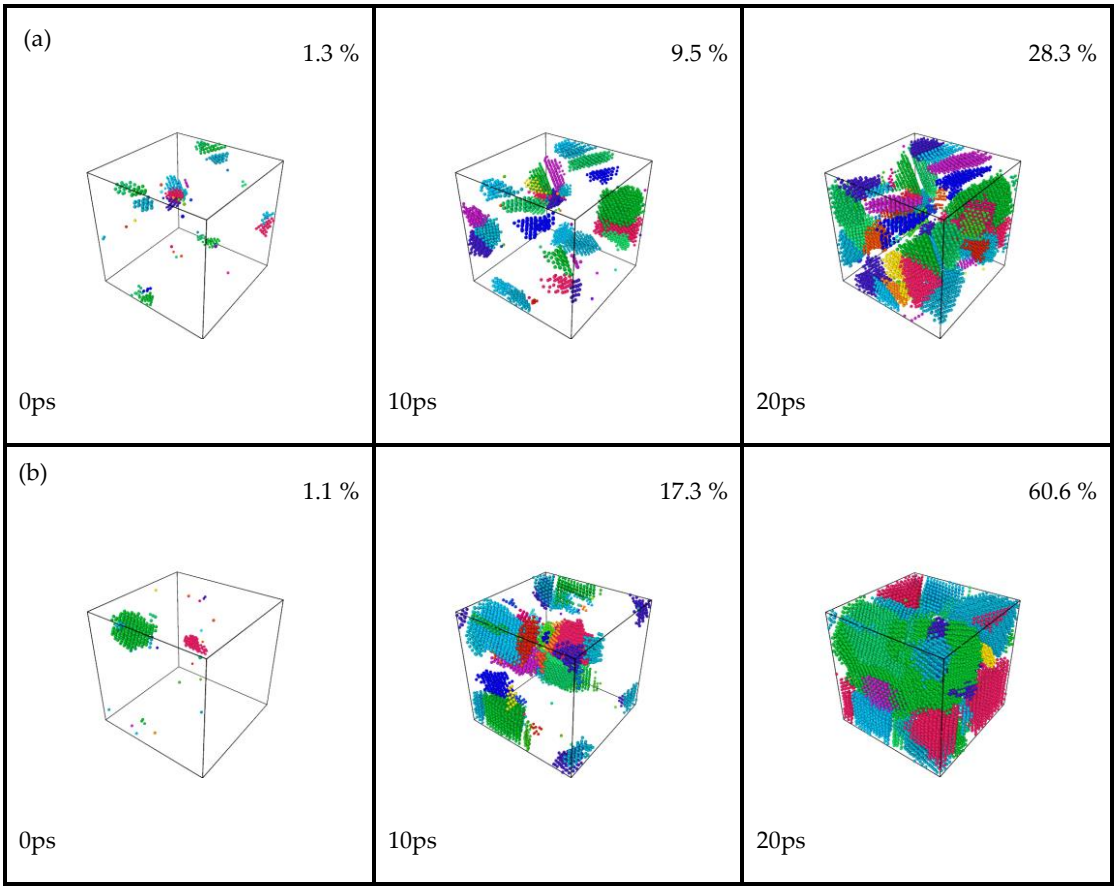

Figure 9. Time evolution snapshots of aluminum alloy crystallization process in different systems; (a) Al-pure and (b) Al-0.3Zr

4. Conclusions

Molecular dynamics simulations and thermodynamic calculations revealed that the introduction of an optimal amount of Zr significantly lowered the nucleation barrier during solidification of aluminum alloy at the atomic level. This reduction in barrier height facilitated the formation of critical crystal nuclei. Additionally, Zr microalloying promoted the transformation of hcp into fcc clusters, resulting in a change in the crystal structure. The growth mechanism of the nucleus was altered, leading to an increase in the solidus temperature of the cast-rolled Al-Mg-Si aluminum alloy and a reduction in the temperature range of the solid-liquid two-phase region. Consequently, there was a substantial enhancement in the solidification rate of the alloy, and the microstructural properties of the alloy after casting and rolling were optimized. By establishing a molecular dynamics model for the corresponding system, this study provides atomic-level mechanistic insights into the influence of Zr microalloying on the solidification rate of cast-rolled Al-Mg-Si aluminum alloy.

It is important to note the limitations of the current molecular dynamics model, which simplifies the complex multicomponent Al-Mg-Si-Mn system to an Al-Zr binary system; therefore, quantitative extrapolation to industrial alloys should be made with caution. Nevertheless, from an industrial perspective, the findings suggest that microalloying with 0.3 wt.% Zr represents an effective strategy to improve the castability and quality of twin-roll cast Al-Mg-Si sheets by mitigating centerline segregation and potentially enabling higher production speeds. The mechanistic understanding of how Zr reduces the nucleation barrier and promotes fcc clustering offers a valuable theoretical foundation for interpreting experimental observations and provides a

https://doi.org/10.64486/m.66.1.2

new perspective for controlling the solidification behavior and microstructure of cast-rolled aluminum alloys in future investigations.

Acknowledgments: This research did not receive any specific grant from funding agencies in the public, commercial, or not-for-profit sectors.

References

[1] A. Arnoldt, L. Semmelrock, D. Soukup and J. A. Österreicher, "Analysis of second phase particles in metals using deep learning: Segmentation of nanoscale dispersoids in 6xxx series aluminum alloys (Al-Mg-Si)," *Mater. Charact*., vol. 191, 112138, 2022. https://doi.org/10.1016/j.matchar.2022.112138

[2] H. M. Jin, D. Tie and R. G. Guan, "Precipitation behavior during re-aging of Al-Mg-Si-Cu alloy," *Mater. Des*., vol. 220, 110883, 2022. https://doi.org/10.1016/j.matdes.2022.110883

[3] X. F. Wang et al., "Influence of asymmetric rolling on the microstructure, texture evolution and mechanical properties of Al–Mg–Si alloy," *Mater. Sci. Eng. A*, vol. 844, 143154, 2022. https://doi.org/10.1016/j.msea.2022.143154

[4] X. Wu et al., "Effect of Cu content on central-segregation composition and mechanical properties of Al–Mg–Si alloys produced by twin-roll casting," *Mater. Sci. Eng. A*, vol. 869, 144782, 2023. https://doi.org/10.1016/j.msea.2023.144782

[5] S. Y. Zhang et al., "Towards relieving center segregation in twin-roll cast Al-Mg-Si-Cu strips by controlling the thermal-mechanical process," *J. Mater. Sci. Technol*., vol. 148, 31–40, 2023. https://doi.org/10.1016/j.jmst.2022.11.023

[6] J. Kuang et al., "Impact of thermal exposure on the microstructure and mechanical properties of a twin-roll cast Al-Mn-Fe-Si strip," *J. Mater. Sci. Technol*., vol. 107, 183–196, 2022. https://doi.org/10.1016/j.jmst.2021.07.022

[7] X. Liu et al., "Effectively mitigated macro-segregation and improved tensile properties of twin-roll casting Al-Cu strips via the addition of TiC nanoparticles," *J. Mater. Process. Technol*., vol. 296, 117200, 2021. https://doi.org/10.1016/j.jmatprotec.2021.117200

[8] J. L. Cann et al., "Sustainability through alloy design: Challenges and opportunities," *Prog. Mater. Sci*., vol. 117, 100722, 2021. https://doi.org/10.1016/j.pmatsci.2020.100722

[9] Y. X. Zhang, H. D. Zhao and F. Liu, "Microstructure characteristics and mechanical properties improvement of gravity cast Al-7Si-0.4Mg alloys with Zr additions," *Mater. Charact*., vol. 176, 111117, 2021. https://doi.org/10.1016/j.matchar.2021.111117

[10] S. W. Pan et al., "Synergistic strengthening by nano-sized α-Al(Mn,Fe)Si and Al_3Zr dispersoids in a heat-resistant Al–Mn–Fe–Si–Zr alloy," *Mater. Sci. Eng*. A, vol. 819, 141460, 2021. https://doi.org/10.1016/j.msea.2021.141460

[11] M. X. Zhang et al., "Enhanced aging precipitation behavior and mechanical properties of 6022 Al-Mg-Si alloy with Zr addition," *Mater. Sci. Eng. A*, vol. 840, 142957, 2022. https://doi.org/10.1016/j.msea.2022.142957

[12] Y. T. Wang et al., "A novel Al-Cr-Sc-Zr alloy additively manufactured via laser directed energy deposition: Microstructure, phase analysis and mechanical properties," *J. Mater. Process. Technol*., vol. 322, 118204, 2023. https://doi.org/10.1016/j.jmatprotec.2023.118204

[13] W. Qian et al., "Microstructure evolution and high-temperature performances of AA6111 alloy strengthened by Sc, Zr co-microalloying," *Mater. Sci. Eng. A*, vol. 887, 145788, 2023. https://doi.org/10.1016/j.msea.2023.145788

[14] Y. F. Wang et al., "Microstructure and strengthening mechanisms of Zr-modified Al–Cu–Mg alloy processed by selective laser melting," *Mater. Sci. Eng. A*, vol. 870, 144874, 2023. https://doi.org/10.1016/j.msea.2023.144874

[15] S. M. Lei, L. Gao, Y. Harada and S. Kumai, "Microstructure and Mechanical Properties of Semi-Solid Die-Cast A356 Aluminum Alloy," *Mater. Sci. Forum*, vol. 877, 39–44, 2016. https://doi.org/10.4028/www.scientific.net/MSF.877.39

https://doi.org/10.64486/m.66.1.2

[16] A. Kolahdooz and S. A. Dehghordi, "Effects of important parameters in the production of Al-A356 alloy by semi-solid forming process," *J. Mater. Res. Technol*., vol. 8, no. 1, 189–198, 2019. https://doi.org/10.1016/j.jmrt.2017.11.005

[17] H. Y. Niu, L. Bonati, P. M. Piaggi and M. Parrinello, "Ab initio phase diagram and nucleation of gallium," *Nat. Commun*., vol. 11, 2654, 2020. https://doi.org/10.1038/s41467-020-16372-9

[18] B. Zhu et al., "The short-range ordering and atomic segregation in various phases of high-entropy alloy during the solidification process," *Mater. Des*., vol. 234, 112290, 2023. https://doi.org/10.1016/j.matdes.2023.112290

[19] M. Moradi-ganjeh, A. Farzadi and A. Ramazani, "Atomic scale melting/solidification behavior and structural evolutions of AlCoCrFeNi high-entropy alloy in selective laser melting process," *J. Mater. Res. Technol*., vol. 27, 6811–6821, 2023. https://doi.org/10.1016/j.jmrt.2023.11.149

[20] G. Azizi, S. Kavousi and M. A. Zaeem, "Interactive effects of interfacial energy anisotropy and solute transport on solidification patterns of Al-Cu alloys," *Acta Mater*., vol. 231, 117859, 2022. https://doi.org/10.1016/j.actamat.2022.117859

[21] G. J. Martyna, D. J. Tobias and M. L. Klein, "Constant pressure molecular dynamics algorithms," *J. Chem. Phys*., vol. 101, no. 5, 4177–4189, 1994. https://doi.org/10.1063/1.467468

[22] R. Fereidonnejad, A. O. Moghaddam and M. Moaddeli, "Modified embedded-atom method interatomic potentials for Al-Ti, Al-Ta, Al-Zr, Al-Nb and Al-Hf binary intermetallic systems," *Comput. Mater. Sci*., vol. 213, 111685, 2022. https://doi.org/10.1016/j.commatsci.2022.111685

[23] B. J. Lee, J. H. Shim and M. I. Baskes, "Semiempirical atomic potentials for the fcc metals Cu, Ag, Au, Ni, Pd, Pt, Al, and Pb based on first and second nearest-neighbor modified embedded atom method," *Phys. Rev. B*, vol. 68, 144112, 2003. https://doi.org/10.1103/PhysRevB.68.144112

[24] E. Asadi, M. A. Zaeem, S. Nouranian and M. I. Baskes, "Two-phase solid–liquid coexistence of Ni, Cu, and Al by molecular dynamics simulations using the modified embedded-atom method," *Acta Mater*., vol. 86, 169–181, 2015. https://doi.org/10.1016/j.actamat.2014.12.010

[25] W. C. Swope, H. C. Andersen, P. H. Berens and K. R. Wilson, "A computer simulation method for the calculation of equilibrium constants for the formation of physical clusters of molecules: Application to small water clusters," *J. Chem. Phys*., vol. 76, no. 1, 637–649, 1982. https://doi.org/10.1063/1.442716

[26] J. W. Liu and S. Kou, "Susceptibility of ternary aluminum alloys to cracking during solidification," *Acta Mater*., vol. 125, 513–523, 2017. https://doi.org/10.1016/j.actamat.2016.12.028

[27] S. Xu et al., "Phase transformations and phase equilibria of a Ti-46.5Al-16.5Nb alloy," *Mater. Des*., vol. 101, 88–94, 2016. https://doi.org/10.1016/j.matdes.2016.03.131

[28] Z. Xu et al., "Effect of Mn/Fe ratio on the microstructure and properties of 6061 sheets obtained by twin-roll cast," *Mater. Charact*., vol. 168, 110536, 2020. https://doi.org/10.1016/j.matchar.2020.110536

[29] E. Giraud, M. Suéry and M. Coret, "High temperature compression behavior of the solid phase resulting from drained compression of a semi-solid 6061 alloy," *Mater. Sci. Eng*. A, vol. 532, 37–43, 2012. https://doi.org/10.1016/j.msea.2011.10.059

[30] Y.C. Sun et al., "Effect of Zr Content on Recrystallization Behavior and Mechanical Properties of Al–Mg–Si Cast-Rolled Sheet", *Acta Metall. Sin*., vol. 62, no. 3, pp. 421–430, 2026, https://doi.org/10.11900/0412.1961.2024.00102

[31] Y.C. Sun et al., "Effect of Mn and Zr Microalloy on the Recrystallization and Solidification Behavior of Cast-Rolled Al-Mg-Si Alloy", *J. Mater. Eng. Perform*., vol. 34, 17333–17343, 2025. https://doi.org/10.1007/s11665-024-10451-4

[32] Y. Sun et al., "Overcoming the time limitation in molecular dynamics simulation of crystal nucleation: a persistent-embryo approach," *Phys. Rev. Lett*., vol. 120, 085703, 2018. https://doi.org/10.1103/PhysRevLett.120.085703

[33] G. C. Sosso et al., "Crystal nucleation in liquids: open questions and future challenges in molecular dynamics simulations," *Chem. Rev.*, vol. 116, no. 12, 7078–7116, 2016. https://doi.org/10.1021/acs.chemrev.5b00744

[34] G. D. Leines, R. Drautz and J. Rogal, "Atomistic insight into the non-classical nucleation mechanism during solidification in Ni," *J. Chem. Phys.*, vol. 146, no. 15, 154702, 2017. https://doi.org/10.1063/1.4980082

[35] J. Bokeloh, R. E. Rozas, J. Horbach and G. Wilde, "Nucleation barriers for the liquid-to-crystal transition in Ni: experiment and simulation," *Phys. Rev. Lett.*, vol. 107, 145701, 2011. https://doi.org/10.1103/PhysRevLett.107.145701

[36] B. Shen et al., "Molecular dynamics simulation studies of structural and dynamical properties of rapidly quenched Al," *J. Non-Cryst. Solids*, vol. 383, 13–20, 2014. https://doi.org/10.1016/j.jnoncrysol.2013.05.004